Acta Mech 230, 449–467 (2019)
https://doi.org/10.1007/s00707-018-2295-z

ORIGINAL PAPER

Ru-Yang Li · Zhi-Wen Cui · Wei-Xi Huang · Li-Hao Zhao · Chun-Xiao Xu

On rotational dynamics of a finite-sized ellipsoidal particle in shear flows

Received: 26 March 2018 / Revised: 30 July 2018 / Published online: 1 November 2018

Abstract The rotational dynamics of finite-sized ellipsoidal particles with different aspect ratios around their fixed mass centers in shear flows have been investigated by direct numerical simulations. Particles are fully resolved by a revised immersed boundary projection method, and their rotational motion is governed by Euler's equation which is calculated in the particle-fixed frame. The particle Reynolds number varies from 10 to 300 based on the longest axis of the particle. The steady states of the prolate and oblate spheroids in uniform flow, linear shear flow with the moving top wall and fixed bottom wall, and wall-bounded turbulence are analyzed. It is observed that the longest particle axes are perpendicular to or have a large angle with the local flow direction in the flow-gradient plane, which leads to a large drag force. A linear stability analysis on the rotational motion of a finite-sized particle in uniform flow is also carried out for supporting this finding. In the linear shear flow, the influence of fluid inertia and fluid shear on the inclined angle is examined in detail. In wall-bounded turbulence, it is found that the particles in the buffer region and the outside of the boundary layer behave similarly in the mean sense as in the linear shear flow and uniform flow, respectively. The present results with intermediate to large particle Reynolds numbers can be regarded as a starting point to understand the dynamics of heavy finite-sized particles in viscous flows.

1 Introduction

Suspended nonspherical particles in shear flows are common in natural and industrial phenomena [34], such as sandstorms near the ground and the papermaking industry. Study of the motion and dynamics of a single ellipsoidal particle is basically the starting point for understanding these processes. As the simplest study, the rotational motion of an isolated, sufficiently small ellipsoidal particle in the Stokes flow was firstly studied analytically by Jeffery [14]. Without particle inertia or fluid inertia, the final rotational state of the particle follows some close orbits (so called Jeffery orbits). However, when particle inertia or the fluid inertia is considered, especially in a turbulent flow, the dynamics of spheroids will be much more complicated.

Several numerical studies concentrating on the rotational motion of a single ellipsoidal particle in the planar Couette flow have been performed. In these studies, the particle inertia and fluid inertia are reflected by the particle Reynolds number $Re_\mathrm{P} = Gd^2/\nu$ (G is the shear rate, d is the major diameter of the particle, and ν is the fluid kinematic viscosity) and the Stokes number $St \sim \alpha Re_P$ (proposed by Lundell and Carksson [22], and α is the solid-to-fluid density ratio). There is a number of investigations concerning the fluid inertia effect by changing Re_P. Ding and Aidun [9] investigated the rotational dynamics of an oblate particle with an aspect ratio (the ratio of polar diameter to equatorial diameter) of AR $= 1/2$ in Couette flow. They found that as Re_P increases, the particle's angular velocity is decreased, while the rotational period is increased. Also, once Re_P is larger than a critical Reynolds number, Re_C, the particle motion turns to a motionless steady state. Their

R.-Y. Li · Z.-W. Cui · W.-X. Huang (✉) · L.-H. Zhao · C.-X. Xu
AML, Department of Engineering Mechanics, Tsinghua University, Beijing 100084, People's Republic of China
E-mail: hwx@tsinghua.edu.cn

findings were later experimentally confirmed by Zettner and Yoda [38]. The same trend of rotational velocity with Re_P was also found in the numerical studies of Qi and Luo [28], Yu et al. [36], Ku and Lin [18], Huang et al. [13], and Mao and Alexeev [23]. In the studies where the motionless state was observed, e.g., Yu et al. [36], Huang et al. [13], and Mao and Alexeev [23], the steady orientation of the ellipsoid is always along its longest axis in the shear plane with a small angle relative to the streamwise direction. Specifically, this small angle is increased with Re_P. On the contrary, for those studies concerning the rotational motion of a center-fixed ellipsoid in the cross-flow, such as Clift et al. [8], Kempe et al. [15], and Ardekani et al. [1,2], the particle tends to reach an equilibrium state with its major axis perpendicular to the local flow, resulting in a maximum drag force at $Re_P = 100$, based on the relative velocity at the particle center and the equivalent particle diameter.

In addition, the effect of the particle inertia was also studied by changing St or the solid-to-fluid density ratio α ([4,9] and [23]). They found that the ellipsoidal particle is forced to rotate around its minor axis by the particle inertia, which is in agreement with the results of Subramanian and Koch [31,32]. In addition, the influence of the initial orientation of the particle has also been considered in Yu et al. [36], Huang et al. (2012), Mao and Alexeev [23], and Rosen et al. [30]. A consistent conclusion was that the oblate particle is insensitive to the initial orientation, whereas the prolate particle tends to reach dramatically different modes with different initial orientations at intermediate to large Re_P.

Recently, the dynamics of ellipsoidal particles in wall-bounded turbulence has also been intensively investigated. Wall-bounded turbulence is much more complicated than the above-mentioned laminar Couette flow because of the nonlinear shear rate, irregular fluctuations, and coherent flow structures in the near-wall region. Studies in turbulent channel flow have received significant attention. Challabotla et al. [5] found that oblate-shaped (inertia-free) tracers preferentially align their symmetry axes normal to the wall, whereas the prolate-shaped tracers were parallel with the wall. In Mortensen et al. [25,26] and Marchioli et al. [24], the inertial prolate particles tend statistically to align themselves to the mean flow direction, and this alignment is increased by increasing the particle aspect ratio. Also, Challatobla et al. [6] showed that the inertial disk-like particles prefer to spin around their symmetry axes in the flow-gradient (shear) plane when located in the near-wall region. In these studies, the Lagrangian point particle method was used, where the translational and rotational dynamics of each particle are governed by the Newton–Euler equations. In these equations, the hydrodynamic force and torque acting on the particles are represented by a drag force formula from Brenner [3] and a torque formula from Jeffery [14], respectively. Both formulas were derived for an ellipsoidal particle in the Stokes flow, which may not correctly reflect the interaction of particles and turbulent flows. In addition, there are also some particle-resolved simulations for finite-sized spherical or ellipsoidal particles suspended in turbulent channel flow by using direct numerical simulation (DNS), e.g., Uhlmann [33], Kempe et al. [16], Ardekani et al. [2] and Eshghinejadfard et al. [10,11]. In Ardekani et al. [2], thousands of neutrally buoyant rigid oblate particles were considered. They found that the particle orientations statistically align their symmetry axes normal to the wall in a similar manner to the inertia-free oblate tracers. In addition, Eshghinejadfard et al. [11] reported that the neutrally buoyant prolate particles show a preferential orientation in the streamwise direction, especially when the particles are close to the wall, leading to the same tendency as the inertia-free prolate tracers.

Although the motionless steady states for a spheroid in both Couette flow and cross-flow at intermediate to large Re_P have become well known, to the best of our knowledge there have been few investigations into the combined effects of fluid inertia and fluid shear on the dynamics of a single spheroid. Also, in the cases calculated by the Lagrangian point particle method in turbulent channel flows, the particle Reynolds number has typically been less than 1 [7], because of the tiny size of the particles. As for the particle-resolved simulations with finite-sized particles [11], the solid-to-fluid density ratio is of order 1, usually neutrally buoyant, which leads to a small relative velocity at the particle center, and thus the particle Reynolds number $Re_P \sim O(10)$. The behavior of a finite-sized heavy particle in wall turbulence at an intermediate to large Re_P is still unresolved.

In the present study, a revised immersed boundary projection method (IBPM) is used to investigate the rotational dynamics of finite-sized ellipsoidal particles in the uniform flow, linear shear flow, and turbulent boundary layer. In contrast to the studies mentioned above, in the present simulation with shear flow the bottom wall is kept stationary, and the top wall is moving in the streamwise direction which facilitates the analysis of the combined effects of fluid inertia and fluid shear. Also, the finite-sized ellipsoidal particles are center-fixed in the flow to simulate the cases at intermediate to large values of Re_P. In the next Section, the governing equation and numerical method will be introduced. Then in Sect. 3, numerical results and discussion will be presented, including the rotational dynamics of a prolate particle and an oblate particle in the uniform flow,

linear shear flow, and wall-bounded turbulence. Specifically, the effects of the flow shear rate, the particle Reynolds number Re_{P}, and the initial orientation will be examined. Finally, conclusions are drawn in Sect. 4.

2 Problem formulation and numerical method

The Navier–Stokes and continuity equations for the incompressible flow are written as:

$$\rho_f\left(\frac{\partial \mathbf{u}}{\partial t}+\mathbf{u}\cdot\nabla\mathbf{u}\right)=-\nabla p+\mu_f\nabla^2\mathbf{u}+\mu_f\mathbf{f},$$
$$\nabla\cdot\mathbf{u}=0, \tag{1}$$

where ρ_f is the fluid density, μ_f is the dynamic viscosity, $\mathbf{u}$ is the fluid velocity, p is the pressure, and $\mathbf{f}$ indicates the additional momentum forcing imposed on the fluid by the particle. Here, this extra term $\mathbf{f}$ is used to satisfy the no-slip condition on the particle surface, which is obtained by the immersed boundary projection method (IBPM) [20].

In the present study, a particle rotating around its fixed mass center is simulated, while the translational motion of the particle is not considered. The rotational motion of a single particle is described by Euler's equation, i.e.,

$$\frac{\mathrm{d}\mathbf{K}_C}{\mathrm{d}t}=\mu_f\oint_{\partial V}\mathbf{r}\times(\boldsymbol{\tau}\cdot\mathbf{n})\mathrm{d}A, \tag{2}$$

where $\mathbf{K}_C$ is the moment of momentum which contains the particle density ρ_P and the particle volume V_P, and $\boldsymbol{\tau}=-p\mathbf{I}+\mu_f(\nabla\mathbf{u}+\nabla\mathbf{u}^{\mathrm{T}})$ is the stress tensor of the fluid. In addition, $\mathbf{I}$ is the unit tensor, and $\mathbf{n}$ is the outwards normal vector on the particle surface.

By integrating Eq. (1) within the region occupied by the particle, it yields

$$\oint_{\partial V}\boldsymbol{\tau}\cdot\mathbf{n}\mathrm{d}A=\oint_{\partial V}\left[-p\mathbf{I}+\mu_f(\nabla\mathbf{u}+\nabla\mathbf{u}^{\mathrm{T}})\right]\cdot\mathbf{n}\mathrm{d}A=-\rho_f\int_{V_P}\mathbf{f}\mathrm{d}V+\rho_f\frac{\mathrm{d}}{\mathrm{d}t}\left(\int_{V_P}\mathbf{u}\mathrm{d}V\right). \tag{3}$$

By substituting Eq. (3) into Eq. (2), we can obtain

$$\frac{\mathrm{d}\mathbf{K}_C}{\mathrm{d}t}+\boldsymbol{\omega}'\times\mathbf{K}_C=-\rho_f\int_{V_P}\mathbf{r}'\times\mathbf{f}'\mathrm{d}V+\rho_f\frac{\mathrm{d}}{\mathrm{d}t}\left(\int_{V_P}\mathbf{r}'\times\mathbf{u}'\mathrm{d}V\right). \tag{4}$$

On the right-hand side of Eq. (4), the first term represents the additional momentum torque exerted on the particle by the surrounding fluid, and the second term indicates the rate of change of the fluid inertia within the region occupied by the particle. For simplification, the rotational motion is solved in the body-fixed coordinate system with the coordinate axes aligned along the principal directions of the moment of inertia of the particle. In Eq. (4), the displacement vector $\mathbf{r}'$, momentum force $\mathbf{f}'$, and fluid velocity $\mathbf{u}'$ are transformed from the inertial frame to the body-fixed frame via a rotation matrix $\mathbf{A}$, i.e., $\mathbf{r}'=\mathbf{A}\mathbf{r}$, $\mathbf{f}'=\mathbf{A}\mathbf{f}$, $\mathbf{u}'=\mathbf{A}\mathbf{u}$, and $\boldsymbol{\omega}'$ denotes the particle's angular velocity in the body-fixed frame. The rotation matrix $\mathbf{A}$ is expressed as

$$\mathbf{A}=\begin{pmatrix}a_{11}&a_{12}&a_{13}\\a_{21}&a_{22}&a_{23}\\a_{31}&a_{32}&a_{33}\end{pmatrix},\quad\begin{aligned}&a_{11}=e_0^2-e_1^2+e_2^2-e_3^2,\ a_{12}=2(e_2e_3+e_0e_1),\\&a_{13}=2(e_1e_2-e_0e_3),\ a_{21}=2(e_2e_3-e_0e_1),\\&a_{22}=e_0^2-e_1^2-e_2^2+e_3^2,\ a_{23}=2(e_1e_3+e_0e_2),\\&a_{31}=2(e_1e_2+e_0e_3),\ a_{32}=2(e_1e_3-e_0e_2),\\&a_{33}=e_0^2+e_1^2-e_2^2-e_3^2\end{aligned} \tag{5}$$

where e_0, e_1, e_2, e_3 are the Euler parameters defined by the Euler angles (ϕ,θ,ψ) as shown in Fig. 6, and $e_0^2+e_1^2+e_2^2+e_3^2=1$. The four Euler parameters are represented as:

$$e_0=\cos\left(\frac{\theta}{2}\right)\cos\left(\frac{\phi+\psi}{2}\right),\quad e_1=\sin\left(\frac{\theta}{2}\right)\cos\left(\frac{\phi-\psi}{2}\right),$$
$$e_2=\sin\left(\frac{\theta}{2}\right)\cos\left(\frac{\phi-\psi}{2}\right),\quad e_3=\cos\left(\frac{\theta}{2}\right)\sin\left(\frac{\phi+\psi}{2}\right). \tag{6}$$

Since the incompressible fluid inside the volume V_P satisfies a rigid body motion at the surface, the torque term representing the fluid inertia inside the volume V_P can be simplified as

$$\frac{\mathrm{d}}{\mathrm{d}t}\left(\int_{V_P}\mathbf{r}'\times\mathbf{u}'\mathrm{d}V\right)=\frac{1}{\rho_P}\frac{\mathrm{d}\mathbf{K}_C}{\mathrm{d}t}. \tag{7}$$

Then, the equation of rotational motion [Eq. (4)] can be written as

$$\left(1-\frac{\rho_f}{\rho_P}\right)\frac{\mathrm{d}\mathbf{K}_C}{\mathrm{d}t}+\boldsymbol{\omega}'\times\mathbf{K}_C=-\rho_f\int_{V_P}\mathbf{r}'\times\mathbf{f}'\mathrm{d}V. \tag{8}$$

We can see that, for the neutrally buoyant case, Eq. (8) cannot be solved, and its original form, i.e., Eq. (4), should be used.

For direct numerical simulation, the Navier–Stokes and continuity equations for incompressible flow are solved by the fractional step method [17], with the pressure, and the additional momentum forcing treated as Lagrange multipliers for enforcing the divergence-free constraint of the flow field and the no-slip condition on the particle surface, respectively. A two-step approximate factorization is utilized to compute the Lagrangian momentum forcing $\mathbf{F}$ on the particle surface and the pressure p consequently, and a high computational efficiency is maintained [20]. Furthermore, the Lagrangian momentum forcing $\mathbf{F}$ is transformed to $\mathbf{f}$ defined on the nearby Eulerian grids by resorting to the discrete delta function [27], i.e.,

$$\mathbf{f}=\sum_l\mathbf{F}_l\delta(\mathbf{x}-\mathbf{X}_l)\Delta V_l. \tag{9}$$

In Eq. (9), $\mathbf{x}$ and $\mathbf{X}_l$ denote the locations of the Eulerian grids and Lagrangian points, and ΔV_l is the volume of the Lagrangian elements. The discrete delta function for 3D cases can be written as:

$$\delta(\mathbf{x}-\mathbf{X}_l)=\frac{1}{(\Delta h)^3}\delta_h\left(\frac{x-X_l}{\Delta h}\right)\delta_h\left(\frac{y-Y_l}{\Delta h}\right)\delta_h\left(\frac{z-Z_l}{\Delta h}\right) \tag{10}$$

where Δh is the size of the Eulerian grids. Here, a four-point smoothed delta function $\delta_h(r)$ is used:

$$\delta_h(r)=\begin{cases}\frac{1}{8h}(3-2\,|r|/\Delta h+\sqrt{1+4\,|r|/\Delta h-4(|r|/\Delta h)^2}) & |r|\le h,\\ \frac{1}{8h}(5-2\,|r|/\Delta h-\sqrt{-7+7\,|r|/\Delta h-4(|r|/\Delta h)^2}) & \Delta h\le|r|\le 2\Delta h,\\ 0. & |r|>2h.\end{cases} \tag{11}$$

Thus, Eq. (4) can be rewritten as

$$\frac{\mathrm{d}\mathbf{K}_C}{\mathrm{d}t}+\boldsymbol{\omega}'\times\mathbf{K}_C=-\rho_f\sum_l\mathbf{r}_l\times\mathbf{F}_l\Delta V_l+\rho_f\frac{\mathrm{d}}{\mathrm{d}t}\left(\int_{V_P}\mathbf{r}'\times\mathbf{u}'\mathrm{d}V\right) \tag{12}$$

or in the discrete form as

$$\begin{aligned}
I_1\frac{\mathrm{d}\omega_1'}{\mathrm{d}t}+(I_3-I_2)\omega_2'\omega_3'&=-\rho_f\sum_l(y'F_z'-z'F_y')\Delta V_l+\rho_f\frac{1}{\Delta t}\left(\int_{V_P}(y'w'-z'v')\mathrm{d}V\right)\Bigg|_{n-1}^{n},\\
I_2\frac{\mathrm{d}\omega_2'}{\mathrm{d}t}+(I_1-I_3)\omega_1'\omega_3'&=-\rho_f\sum_l(z'F_x'-x'F_z')\Delta V_l+\rho_f\frac{1}{\Delta t}\left(\int_{V_P}(z'u'-x'w')\mathrm{d}V\right)\Bigg|_{n-1}^{n},\\
I_3\frac{\mathrm{d}\omega_3'}{\mathrm{d}t}+(I_2-I_1)\omega_1'\omega_2'&=-\rho_f\sum_l(x'F_y'-y'F_x')\Delta V_l+\rho_f\frac{1}{\Delta t}\left(\int_{V_P}(x'v'-y'u')\mathrm{d}V\right)\Bigg|_{n-1}^{n}.
\end{aligned} \tag{13}$$

Then, Eq. (13) is solved by using the classical fourth-order Runge–Kutta method.

After obtaining the angular velocity of the particle, the velocity at each Lagrangian point on the particle surface can be calculated by $\mathbf{U}'_P(\mathbf{x}) = \boldsymbol{\omega}' \times \mathbf{r}'(\mathbf{x})$, and the fluid velocity $\mathbf{u}' = \mathbf{U}'_P(\mathbf{x})$ on the particle surface is obtained from the no-slip condition. Moreover, we can obtain the rate of change of the Euler parameters by using the rotational velocity, i.e.,

$$\begin{pmatrix} \dot{e}_0 \\ \dot{e}_1 \\ \dot{e}_2 \\ \dot{e}_3 \end{pmatrix} = \frac{1}{2} \begin{pmatrix} e_0 & -e_2 & -e_3 & -e_1 \\ e_1 & -e_3 & e_2 & e_0 \\ e_2 & e_0 & -e_1 & e_3 \\ e_3 & e_1 & e_3 & -e_2 \end{pmatrix} \begin{pmatrix} 0 \\ \omega'_1 \\ \omega'_2 \\ \omega' \end{pmatrix}, \tag{14}$$

which is used to update the rotation matrix for the next time step.

3 Results and discussion

3.1 Numerical validation

Two test cases are presented here to validate our numerical method in solving the dynamics of finite-sized particles in viscous fluid. Specifically, the case of an ellipsoid rotating freely in a linear shear flow is considered for testing the ability in resolving the rotational motion, and that in uniform flow is also tested to see whether the current method is able to capture the motion of ellipsoids at an intermediate Reynolds number.

3.1.1 Example 1: rotational motion of an ellipsoid in linear shear flow

Firstly, the rotational motion of an ellipsoid in linear shear flow is simulated to compare with the analytical solution given by Jeffery [14] in the Stokes flow regime. The cases of a prolate particle with an aspect ratio (the ratio of polar diameter to equatorial diameter) AR $= 3$ and an oblate particle with AR $= 1/3$ have been considered. The major diameters (i.e., the longest axes) for both ellipsoids are $L = 1.0$, and the computational domain has a range of $[-4L, 4L] \times [-4L, 4L] \times [-4L, 4L]$ in the streamwise (x), wall-normal (y), and spanwise (z) directions, respectively. The mesh size is $256 \times 256 \times 256$ with 32 uniform grids per L, and the particle surface is discretized by 1538 triangular unstructured grids generated by the subdivision method [12]. The linear shear flow is generated by moving the top wall and the bottom wall in the opposite directions with the same speed U, and the shear rate is set to be $G = 0.05$. The periodic boundary condition is imposed in the spanwise (z) direction, and the Dirichlet boundary condition ($u = Gy, v = w = 0$) is used at the inlet, while the convective boundary condition is applied at the outlet. The corresponding particle Reynolds number is $Re_P = 0.1$, which is defined as $Re_P = GL^2/\nu$. The particle is located at the center of the domain, where the local velocity is zero. The initial orientation for both particles is set as $(\phi_0, \theta_0, \psi_0) = (0, \pi/4, 0)$, and the particles tumble in the flow-gradient plane periodically after releasing. The orientation angle (0, 0, 0) represents that the symmetry axis of the particle orients in the wall-normal (y) direction. Figure 1 shows the time histories of the rotational velocities in the spanwise direction for both particles. It is found that, for both prolate and oblate spheroids, the present numerical results and the theoretical solutions are in good agreement, thus validating the present method in solving the rotational motion of the ellipsoids.

3.1.2 Example 2: rotational motion of an oblate particle in uniform flow

In addition to the test case of a particle freely rotating in the Stokes flow, here a series of numerical simulations is performed in a uniform flow at a finite Re_P. The computation domain ranges $[-4L, 12L] \times [-4L, 4L] \times [-4L, 4L]$ with 32 uniform grids per L, i.e., the major diameter of the oblate particle. The uniform inflow ($u = 1.0, v = w = 0$) is imposed at the inlet, and the convective condition is applied at the outlet. Moreover, the Dirichlet condition is used at the top and bottom walls, and the periodic condition is adopted in the spanwise direction. The oblate particle with AR $= 1/2.5$ freely rotates around its center, which is fixed at $x = 0$ in the streamwise direction, and at the middle of the spanwise and wall-normal directions. The particle Reynolds number is $Re_P = 100$ based on the relative velocity U_P at the particle center, which is measured at the same height of the incoming flow, and the major diameter L of the oblate particle. The solid-to-fluid density ratio (α) varies from 2 to 16. As shown in Fig. 2, the time histories of the angle between the symmetry axis and the streamwise direction from the present simulations are compared with those of Ardekani et al. [1,2], and

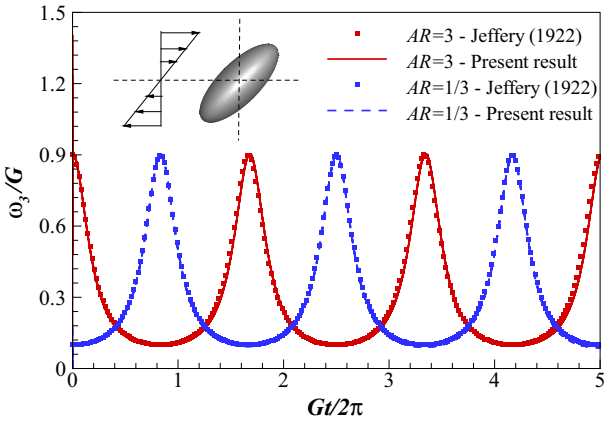

Fig. 1 Time histories of the spanwise angular velocity of spheroids with aspect ratios of 3 and 1/3 in a linear shear flow. The present results are compared with the analytical solution by Jeffery [14]

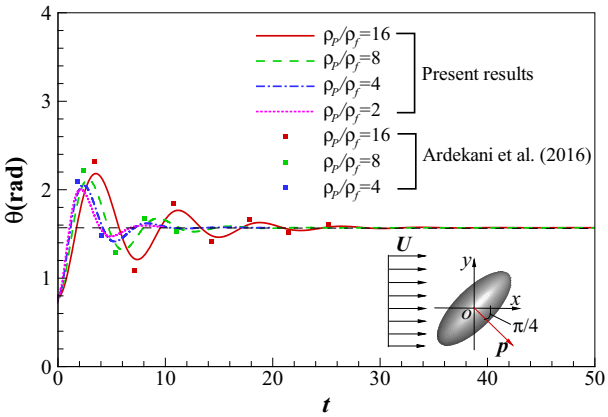

Fig. 2 Time histories of the angle between the symmetry axis of an oblate particle and the wall-normal direction for different density ratios

a satisfactory agreement is found. It can be seen that the amplitude and period of the angle variations are decayed as time goes by and are increased with the increasing density ratio. Interestingly, the present results show that the oblate particle freely rotating in the uniform flow has an equilibrium state with its symmetry axis aligning with the streamwise direction, leading to the maximum drag force, which is consistent with the previous findings by Clift et al. [8], Kempe et al. [15], and Ardekani et al. [1,2].

3.2 Rotational dynamics of an ellipsoid in uniform flow

Considering the preceding test case of an oblate particle in uniform flow, the effect of the initial orientation is further examined. The solid-to-fluid density ratio is fixed at $\alpha = 10.0$, and the particle Reynolds number is set as $Re_P = 100$. The particle is released from rest, with its center-fixed at the original point. The parameters for computational domain, mesh resolution, and boundary conditions are the same as in the validation case in a uniform flow in Sect. 3.1.2. Two types of particles are considered, and the parameters of the particle shape and the initial orientation are listed in Table 1.

Figure 3a shows the time histories of the orientation angles $(\theta_x, \theta_y, \theta_z)$ between the symmetry axis of the oblate particle and the global coordinate axes. With four different combinations of the initial orientations listed in Table 1, the oblate particles all converge to the same steady motionless state, in which their symmetry axes align along the streamwise direction, and Fig. 3a represents the results of case 3b as an example. The angles between the symmetry axis and the x-axis (θ_x) converge to nearly 0 or 180°, whereas both θ_y and θ_z converge to 90°.

Table 1 Computational parameters for simulations of an ellipsoidal particle in uniform flow and its orientation at the steady state

Case	Aspect ratio	Initial Euler angles (ϕ, θ, ψ)	Initial direction of symmetry axis
1a	2.5 (prolate)	(0, 0, 0)	Along the y-axis
2a		$(0, \pi/4, 0)$	In the flow-gradient plane
3a		$(\pi/4, \pi/4, 0)$	Inclined orientation
4a		$(\pi/2, \pi/2, 0)$	Along the z-axis
1b	1/2.5 (oblate)	(0, 0, 0)	Along the y-axis
2b		$(0, \pi/4, 0)$	In the flow-gradient plane
3b		$(\pi/4, \pi/4, 0)$	Inclined orientation
4b		$(\pi/2, \pi/2, 0)$	Along the z-axis

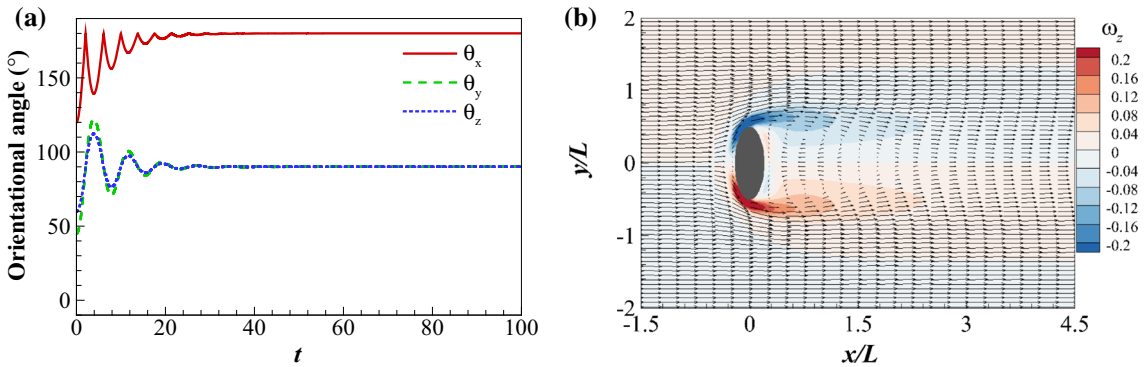

Fig. 3 **a** Orientation angles between the symmetry axis and the global coordinates axes; **b** contours of the spanwise vorticity and velocity vectors around an oblate particle (AR = 1/2.5) in the $x - y$ plane

A similar phenomenon is shown for the prolate particles in Fig. 4a, c, which shows the results of case 2a and case 4a. It is observed that the prolate particles also achieve a steady state with their symmetry axes perpendicular to the flow direction with the maximum drag force. For a prolate particle, it tends to have two different steady states depending on the initial orientation. When the particle is released with its symmetry axis close to the y-axis like the case 1a, or in the flow-gradient plane like case 2a, it converges to a motionless state with its symmetry axis pointing to the y-axis. In addition, the symmetry axis of a prolate particle aligns along the z-axis without rotation when its initial orientation is close to the z-axis direction, like case 4a. It should be noted that there is no preference of the orientation direction in the $y - z$ plane by setting the uniform incoming flow, and the converged orientation along the y- or z-axis indicates that the influence of the computational domain boundary is not negligible in the present simulations. Nevertheless, the main fluid–solid interaction feature is well captured, i.e., that the major diameter is always perpendicular to the flow direction for both the oblate and prolate ellipsoids, which can also be confirmed by the linear stability analysis, as presented in the Appendix. Moreover, Figs. 3b and 4b, d display the instantaneous fields of the spanwise vorticity and velocity vectors around the particle in the $x - y$ plane. The distributions of the velocities and vorticities around the particles are quite symmetric, which verify the steady states of the ellipsoidal particles.

3.3 Rotational dynamics of an ellipsoid in linear shear flow

In this Section, the dynamics of an ellipsoidal particle in a linear shear flow is simulated to investigate the combined effects of fluid inertia and fluid shear on the dynamics of a single ellipsoid. Previous studies pointed out that when an ellipsoid in Couette flow reaches a motionless steady state it will preferentially align its major axis close to the local flow direction with the minimum drag force ([13,23,36]). On the contrary, an ellipsoidal particle in uniform flow tends to align its major axis perpendicular to the streamwise direction with the maximum drag force ([1,2,8,15]), as shown in Sect. 3.2. Therefore, it reflects that the effects of the fluid shear stress and fluid inertia are resisting each other.

Different from the previous studies using Couette flow with two opposite moving walls, the present shear flow is generated by moving the top wall at a speed of U while fixing the bottom wall, as sketched in Fig.

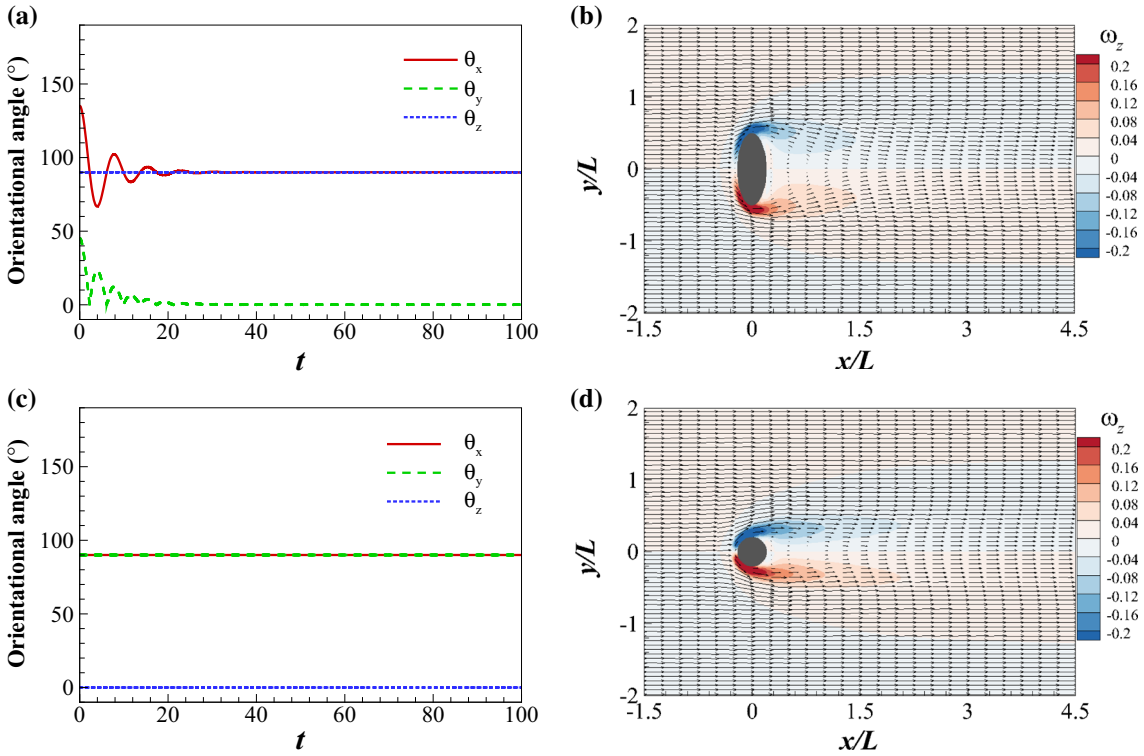

Fig. 4 **a**, **c** Orientation angles between the symmetry axis and the coordinates axes of the global coordinate system; **b**, **d** contours of the spanwise vorticity and velocity vectors around for a prolate particle (AR = 2.5) in the $x - y$ plane. **a** and **b** are related to the steady state with its symmetry axis aligning with the y-axis direction; **c** and **d** are related to the steady state with its symmetry axis aligning with the z-axis direction

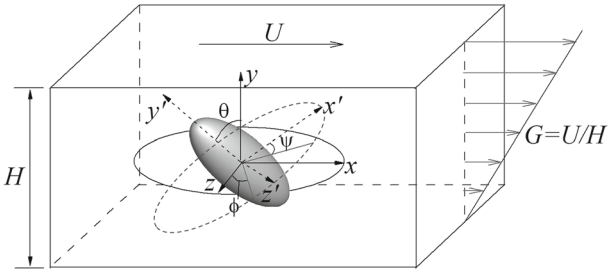

Fig. 5 Schematic of a spheroidal particle rotating freely around its fixed center in a linear shear flow. The bottom wall is fixed, and the top wall is moving with a constant velocity U. φ, θ and ψ are the Euler angles which represent the orientation of the spheroid. (x, y, z) is the global coordinates, and (x', y', z') is the body-fixed coordinates

5. Similar to the validation cases in linear shear flow, the periodic boundary condition is imposed in the spanwise (z) direction, and the Dirichlet boundary condition ($u = Gy, v = w = 0$) is used at the inlet, while the convective boundary condition is applied at the outlet. The particle Reynolds number is defined as $Re_P = U_P L/\nu$, based on the relative velocity U_P at the particle center and the major diameter L of the particle. The present shear flow can be divided into two parts: the uniform flow with a velocity of $U/2$ and the Couette flow with the two walls moving at a speed of $U/2$ and $-U/2$, respectively, which can be used to study the combined effects of fluid inertia and fluid shear.

To verify both effects on the particle dynamics, a series of numerical simulations is conducted systematically. Here the fluid inertia and the shear rate are varied separately to avoid the interference of each other. When considering the effect of fluid inertia, the shear rate is fixed. The computational parameters for the cases of a fixed shear rate $G = 0.25$ are listed in Table 2, where the major diameter of the ellipsoid is denoted by $L = 1.0$ and the moving velocity of the top wall is fixed at $U = 1.0$. The computational domain ranges $[-4L, 12L] \times [0, 4L] \times [-2L, 2L]$ with 32 uniform grids per L. The particle center is located at $x = 0$, $z = 0$.

Table 2 Computational parameters for the simulations with a fixed shear rate, $G = 0.25$

Case	Computational domain height (H)	Velocity of top wall (U)	Particle location (y_c)	Fluid velocity at the particle center (U_p)
1	$4L$	1.0	$1.5L$	0.375
2			$1.75L$	0.4375
3			$2L$	0.5
4			$2.25L$	0.5625
5			$2.5L$	0.625

Table 3 Computational parameters for the simulations with a fixed relative velocity at the particle center, $U_P = 0.5$

Case	Computational domain height (H)	Velocity of top wall (U)	Particle location (y_c)	Flow shear rate (G)
1	$8L$	0.8	$5L$	0.1
2	$6.25L$	1.0	$3.125L$	0.16
3	$4L$	1.0	$2L$	0.25
4	$3.125L$	1.0	$1.5625L$	0.32
5	$3L$	1.2	$1.25L$	0.4

By locating the particle center at different heights, the relative velocity is changed correspondingly, which leads to a change of the fluid inertia. On the other hand, for analyzing the effect of the shear rate, the fluid inertia is kept the same by fixing the relative velocity at the particle center, $U_P = 0.5$. The computational parameters are listed in Table 3, where the height of the computational domain, the moving velocity of the top wall, and the position of the particle center are confined to different combinations to ensure the same relative velocity at the particle center, but with different shear rates. Moreover, the fluid kinematic viscosity is varied in simulations, i.e., $\nu = 1/360$ and 1/600 for larger Re_P and $\nu = 1/20$ and 1/40 for smaller Re_P. Here the prolate particle of AR $= 3$ and oblate particle of AR $= 1/3$ are considered, and the solid-to-fluid density ratio is fixed at $\alpha = 10.0$. The initial orientation for the prolate particles is set as $(\phi_0, \theta_0, \psi_0) = (0, \pi/4, 0)$ and $(\phi_0, \theta_0, \psi_0) = (\pi/4, \pi/4, 0)$ for the oblate particles.

Figure 6 shows the orientations of an oblate particle in a linear shear flow, and the instantaneous distributions of the spanwise vorticity and the velocity vector around the particle in the $x - y$ plane are also presented. Two different viscosities, i.e., $\nu = 1/20$ and 1/360, are compared, with the shear rate $G = 0.25$ and the relative velocity at the particle center $U_P = 0.5$. Figure 6 shows the results for an oblate particle with the computational parameters of case 3 in Table 2 (also in Table 3). The oblate particle in the present linear shear flow reaches a motionless state where its symmetry axis is aligned close to the streamwise direction with a large drag force, which can be regarded as the combination of equilibrium states for an oblate particle in the uniform flow and Couette flow. The fluid inertia dominates the motionless state, while the fluid shear urges the oblate particle to deviate from this maximum drag state with a small inclined angle (namely the angle between the symmetry axis of the oblate particle and the streamwise direction). The symmetry axis of the oblate particle is nearly perpendicular to the spanwise direction for both cases at $\nu = 1/20$ and 1/360, while the inclined angle in the flow-gradient plane increases with increasing viscosity from 10.7° at $\nu = 1/360$ (large Re_P) to 24.7° at $\nu = 1/20$ (small Re_P). This observation can be attributed to the enhancement of the shear stress with a higher fluid viscosity. By comparing Figs. 6b, d, it is obvious that for large viscosity with a small Re_P the recirculation zone is confined to a small region behind the particle with a stronger torque, which also results in a larger inclined angle.

Similarly, Fig. 7 shows the orientation and the instantaneous field for a prolate particle as shown in Fig. 6, and also the parameter combination of case 3 in Table 2 (also in Table 3) is chosen. Different from the oblate particle, the dynamics of the prolate particle is sensitive to the local flow conditions and does not stay at a motionless state at large Re_P. Figure 7c shows a typical evolution of the orientation for the prolate particle at large Re_P, where the orientation angle between the symmetry axis and the z-axis is varied periodically. By projecting the symmetry axis of the prolate particle to the flow-gradient plane, there also exists a stable inclined angle (namely the angle between the symmetry axis of a prolate particle and the wall-normal direction). That is to say, the prolate particle has an average inclined angle in the flow-gradient plane with a periodic swing

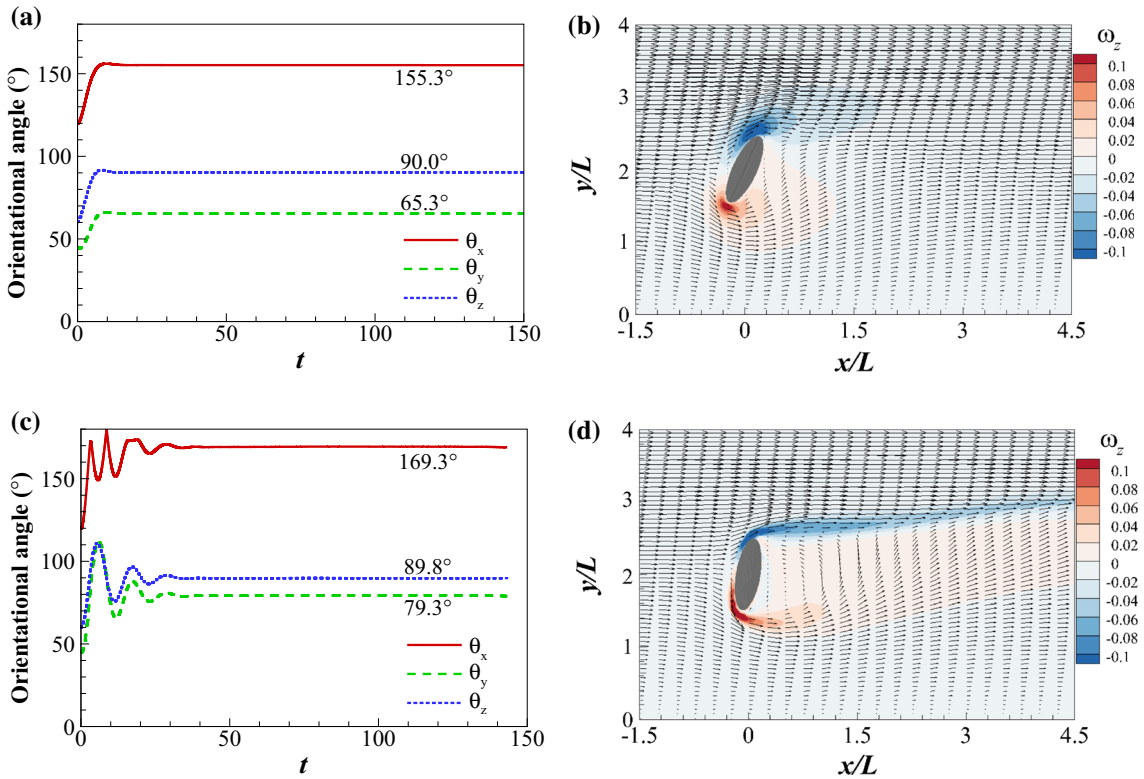

Fig. 6 **a**, **c** Orientation angles between the symmetry axis and the global coordinates axes; **b**, **d** contours of the spanwise vorticity and velocity vectors around an oblate particle (AR $= 1/3$) in the $x - y$ plane. In **a**, **b** the viscosity is $\nu = 1/20$, and in **c**, **d** $\nu = 1/360$. The shear rate is $G = 0.25$, and the relative velocity at the particle center is $U_{\mathrm{P}} = 0.5$

motion in the spanwise direction. In addition, the prolate particle has the same dependency of the inclined angle on the fluid viscosity as the oblate particle, varying from 11.2° at $\nu = 1/360$ (large Re_{P}) to 36.8° at $\nu = 1/20$ (small Re_{P}).

Specifically, the prolate particle in the flow with a larger shear rate and a higher viscosity, that is to say, with a much larger shear stress, converges to a quite different steady state. Figure 8 shows the results with the fluid viscosity of $\nu = 1/20$, the shear rate $G = 0.4$, and the relative velocity at the particle center $U_{\mathrm{P}} = 0.5$, which corresponds to case 5 in Table 3. After a long transition stage, the prolate particle tends to align its symmetry axis to the spanwise direction and rotate about its symmetry axis, which is called log-rolling [19] and is usually observed in Couette flow ([13,36]). In this case, the fluid shear effect dominates the rotational dynamics of the prolate particles.

Furthermore, the dependencies of the inclined angle on the shear rate G and the relative velocity U_{P} at the particle center are analyzed. Figure 9 represents the variations in the inclined angle as a function of U_{P} with a fixed shear rate $G = 0.25$ and different fluid viscosities. It is observed that the inclined angle is decreased for both prolate particles and oblate particles as U_{P} increases. The increased fluid inertia forces the particles to reach a motionless state, in which its major diameter tends to be perpendicular to the local flow direction with a large drag force, i.e., a smaller inclined angle. As the fluid viscosity increases, the inclined angle of the prolate particle is also increased due to the enhanced shear stress by comparing Figs. 9a, b. When the fluid viscosity is relatively low, as shown in Fig. 9a, the oblate particle is insensitive to the change of fluid viscosity, and the declination of the inclined angle is much milder than that for prolate particles. On the other hand, the inclined angle of the oblate particle is increased with the increasing fluid viscosity for relatively high fluid viscosities, as shown in Fig. 9b, and the tendency is similar to that of the prolate particle. But there exists no linear dependence of the inclined angles on either fluid inertia or fluid shear.

Figure 10 shows the variations in the inclined angle as a function of G with a fixed relative velocity at the particle center $U_{\mathrm{P}} = 0.5$ and different fluid viscosities. It is seen that the inclined angle is increased with shear rate G for both prolate and oblate particles, because the shear stress forces the particle to reach a steady state with its major diameter aligned close to the streamwise direction. This tendency is opposite to the effect

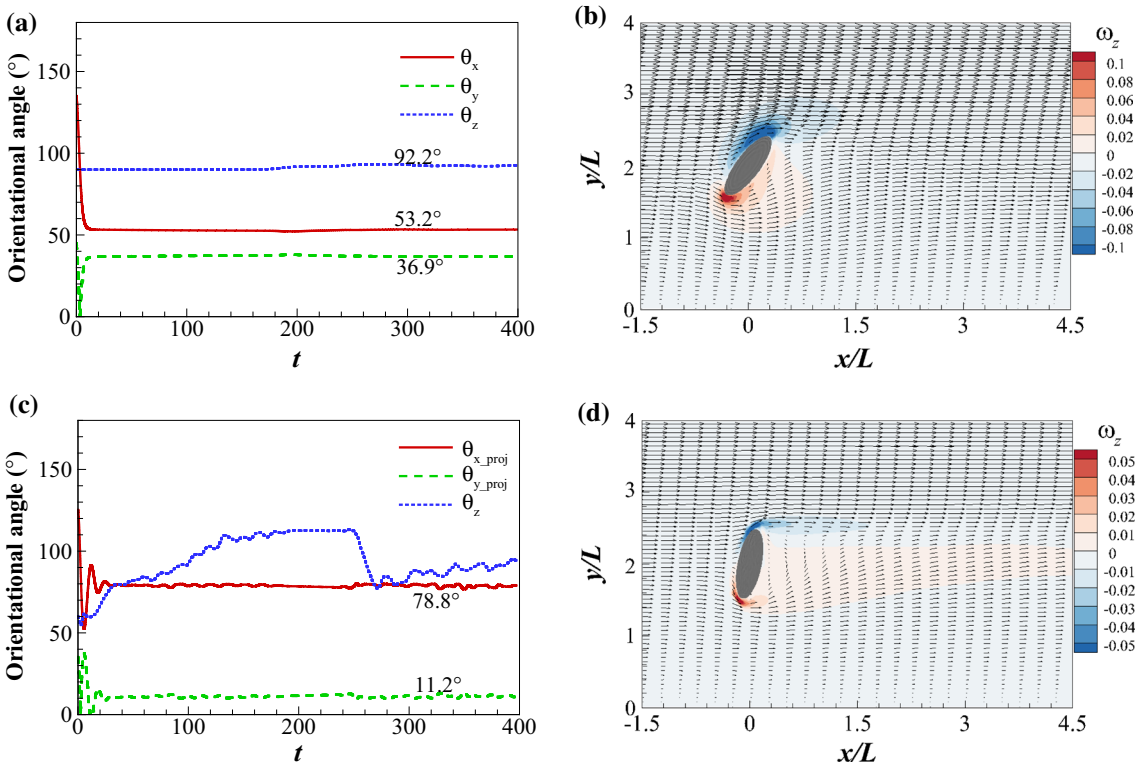

Fig. 7 **a**, **c** Orientation angles between the symmetry axis and the global coordinates axes; **b**, **d** contours of the spanwise vorticity and velocity vectors around a prolate particle (AR = 3) in the $x-y$ plane. In **a**, **b** the viscosity is $\nu = 1/20$, and in **c**, **d** $\nu = 1/360$. The shear rate is $G = 0.25$, and the relative velocity at the particle center is $U_P = 0.5$. The "x_proj" and "y_proj" in **c** represent the orientation angles between the projected symmetry axis in the $x-y$ plane and the x-axis/y-axis of the global coordinate system

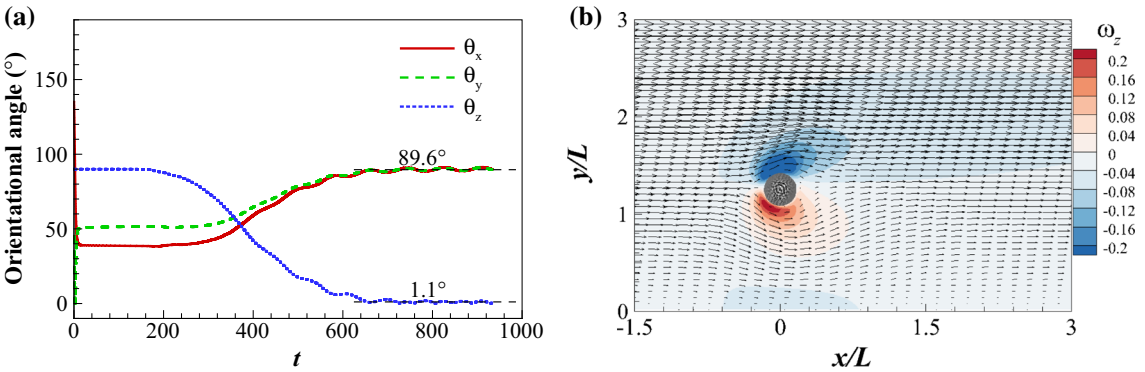

Fig. 8 **a** Orientation angles between the symmetry axis and the coordinates axes of the global coordinate system; **b** contours of the spanwise vorticity and velocity vectors around a prolate particle (AR = 3) in the $x-y$ plane. The fluid viscosity is $\nu = 1/20$, the shear rate is $G = 0.4$, and the relative velocity at the particle center is $U_P = 0.5$. At the steady state, the prolate particle rotates with a constant rotational rate with its symmetry axis aligned with the z-axis

of fluid inertia as shown in Fig. 9. Moreover, as the fluid viscosity increases, the inclined angle of the prolate particle is also increased, by comparing Fig. 10a with b. The oblate particles are insensitive to the change of relatively low viscosities (Fig. 10a), but for higher viscosities the inclined angles show a significant increase with increasing viscosity (Fig. 10b). Specifically, with the highest viscosity $\nu = 1/20$ and the largest shear ratio $G = 0.4$ considered in the present study, as shown in Fig. 10b, the prolate particle does not sustain an inclined position in the flow-gradient plane, but is transferred to a new orientation, rotating around its symmetry axis, which is along the spanwise direction (Fig. 8).

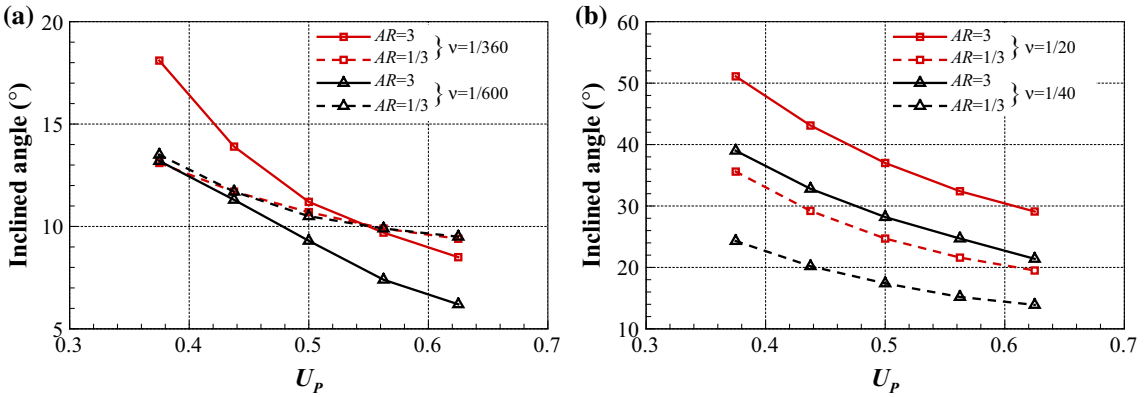

Fig. 9 Variations in the inclined angles between the symmetry axis of the spheroid and y-axis (for the prolate particle, AR = 3) or the x-axis (for the oblate particle, AR = 1/3) as a function of U_P: **a** the cases of relatively low fluid viscosities, and **b** the cases of relatively high fluid viscosities

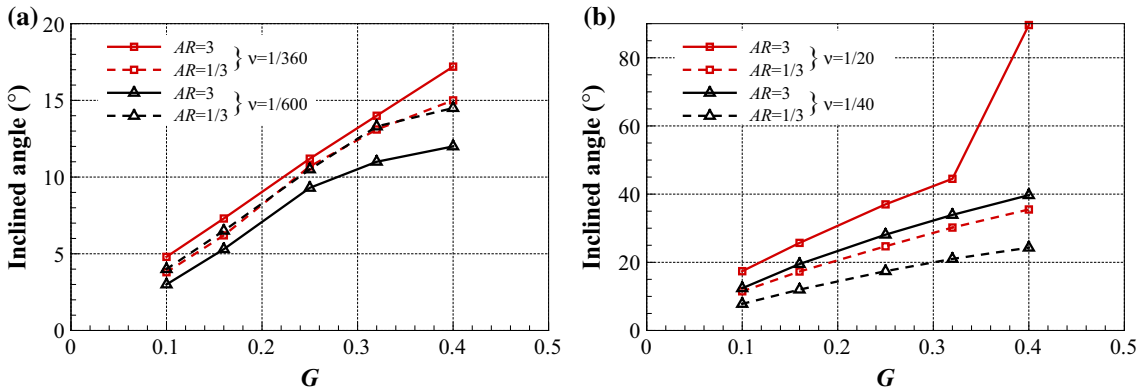

Fig. 10 Variations in the inclined angles between the symmetry axis of the spheroid and the y-axis (for the prolate particle, AR = 3) or the x-axis (for the oblate particle, AR = 1/3) as a function of the shear rate: **a** the cases of relatively low fluid viscosities, and **b** the cases of relatively high fluid viscosities

3.4 Rotational dynamics of an ellipsoid in wall-bounded turbulence

In the preceding case of an ellipsoid in a linear shear flow, the combined effect of fluid inertia and fluid shear has been intensively discussed, and here a more complex, but real situation of an ellipsoid rotating freely in wall-bounded turbulence is considered. In wall-bounded turbulence, especially in the near-wall region, the fluid motion is nonlinear, and the turbulent fluctuations are intensive. In the previous studies, the dynamics of ellipsoidal particles in turbulent channel flow were extensively explored ([6], Ardekani et al. [2] and [10,11]), but rarely in turbulent boundary layer.

The rotational dynamics of two differently shaped finite-sized ellipsoids with aspect ratios of AR = 1/3 and 3 around their fixed mass centers in wall-bounded turbulence are further investigated. The turbulent circumstance is provided by a fully developed turbulent boundary layer with fluid viscosity $\nu = 1/360$, and the cases of particles at different heights are considered. The major diameter of the ellipsoid L is set to be equal to the momentum thickness of the turbulent boundary layer at the inlet. The computational domain is $[0, 64L] \times [0, 30L] \times [-16L, 16L]$ in the streamwise (x), wall-normal (y) and spanwise (z) direction, respectively. The particle center is located at $x = 10L$ in the streamwise direction and in the centerline of the spanwise direction. Direct numerical simulations of the spatially developed turbulent boundary layer are performed, with a friction Reynolds number $Re_\tau = 181$ based on the friction velocity u_τ and the boundary layer thickness δ at $x = 10L$. The boundary layer thickness δ at the inlet and at $x = 10L$ equals $9.42L$ and $9.66L$, respectively. The particle Reynolds number is defined as $Re_P = U_P L/\nu$, based on the relative velocity at the particle center and the major diameter of the particle. The particle is placed in the buffer layer ($y_P = L$ or $y_P^+ = 18.1$) with a local particle Reynolds number of $Re_P = 180$, or outside of the boundary

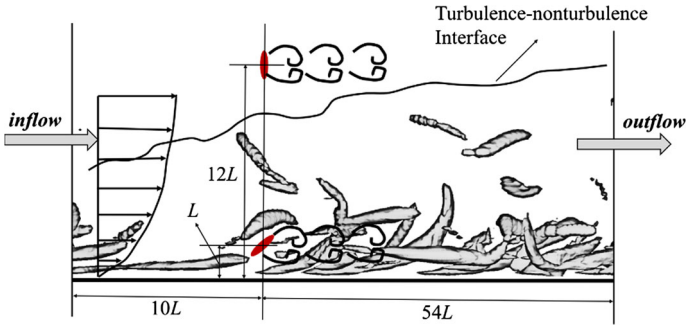

Fig. 11 Schematics of an ellipsoid rotating freely around its fixed center in wall-bounded turbulence

Table 4 Computational parameters for the simulations of an ellipsoid in wall-bounded turbulence and its orientation at the steady state

Case	Aspect ratio	Initial Euler Angles (ϕ, θ, ψ)	Direction of symmetry axes	Particle locations
1a	3 (prolate)	(0, 0, 0)	Along the y-axis	$y_c = L$ (buffer region) or $12L$ (outside of the boundary layer)
2a		$(\pi/6, \pi/6, 0)$	Close to the y-axis	
3a		$(\pi/3, \pi/3, 0)$	Close to the z-axis	
4a		$(0, \pi/2, 0)$	Along the x-axis	
5a		$(\pi/2, \pi/2, 0)$	Along the z-axis	
1b	1/3 (oblate)	(0, 0, 0)	Along the y-axis	
2b		$(\pi/6, \pi/6, 0)$	Close to the y-axis	
3b		$(\pi/3, \pi/3, 0)$	Close to the z-axis	
4b		$(0, \pi/2, 0)$	Along the x-axis	
5b		$(\pi/2, \pi/2, 0)$	Along the z-axis	

layer ($y_P = 12L$ or $y_P^+ = 217.2$) with a local particle Reynolds number of about $Re_P = 360$. As for the computational resolution, 2048 and 1024 grids are uniformly distributed in the streamwise and spanwise directions, respectively, with 32 uniform grids per L. In the wall-normal direction, 150 and 178 grids are used to resolve the cases for a particle located in the buffer region and outside of the boundary layer, respectively. The grids are refined locally in the near-wall region and in the vicinity of the particle and are stretched for other regions. The inflow–outflow condition is applied in the streamwise direction, and the inflow velocity profile is obtained by an auxiliary turbulent boundary layer simulation without a particle, based on a rescaling method [21]. Validations of direct numerical simulation of the pure turbulent boundary layer can be found in our previous study [35]. The schematics of the present computational setup are shown in Fig. 11. The density ratio of the ellipsoids to fluid flow is fixed at $\alpha = 10.0$, and five different initial orientations are chosen for each particle. The computational parameters for the simulations are listed in Table 4.

For an ellipsoidal particle positioned in the buffer layer, where the turbulent fluctuation and shear stress are both intensive, its orientation changes dramatically as compared with those in the uniform flow and linear shear flow. Figures 12 and 13 show the time histories of the orientation angles of the symmetry axes of prolate and oblate particles, respectively. Variations in the amplitude and period of the orientation angle can be attributed to the turbulent fluctuations and the near-wall flow structures, as displayed in Fig. 14, though in such complex circumstances the prolate and oblate particles still have an average steady state similar to that in the linear shear flow.

In Fig. 12, the results of case 3b in Table 4 are represented as an example, where the oblate particle tends to align its major diameter nearly perpendicular to the streamwise direction with a large drag force. As shown in Fig. 12a, the average inclined angle for the oblate particle is around 10° which is comparable with that in the linear shear flow. In Fig. 13, the prolate particle also aligns its major diameter nearly perpendicular to the local flow direction, while its initial orientation has influence on the average steady orientation. When its initial orientation is close to the normal-wall (y) direction, i.e., cases 1a and 2a in Table 4, the prolate particle converges to an averaged steady alignment close to the wall-normal direction with a slight inclination angle in the flow-gradient plane, and Fig. 13a shows the results of case 1a. The averaged inclined angle is about 12°, and this is also comparable with that in the linear shear flow. Meanwhile, for the prolate particle initially

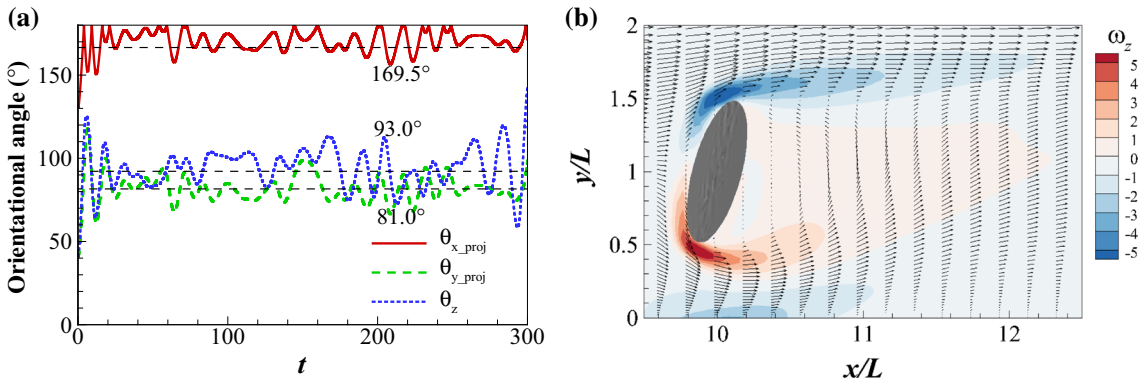

Fig. 12 **a** Orientation angles between the symmetry axis and the global coordinates axes and **b** contours of the spanwise vorticity and velocity vectors in the $x - y$ plane for an oblate particle (AR $= 1/3$) located in the buffer region of the turbulent boundary layer

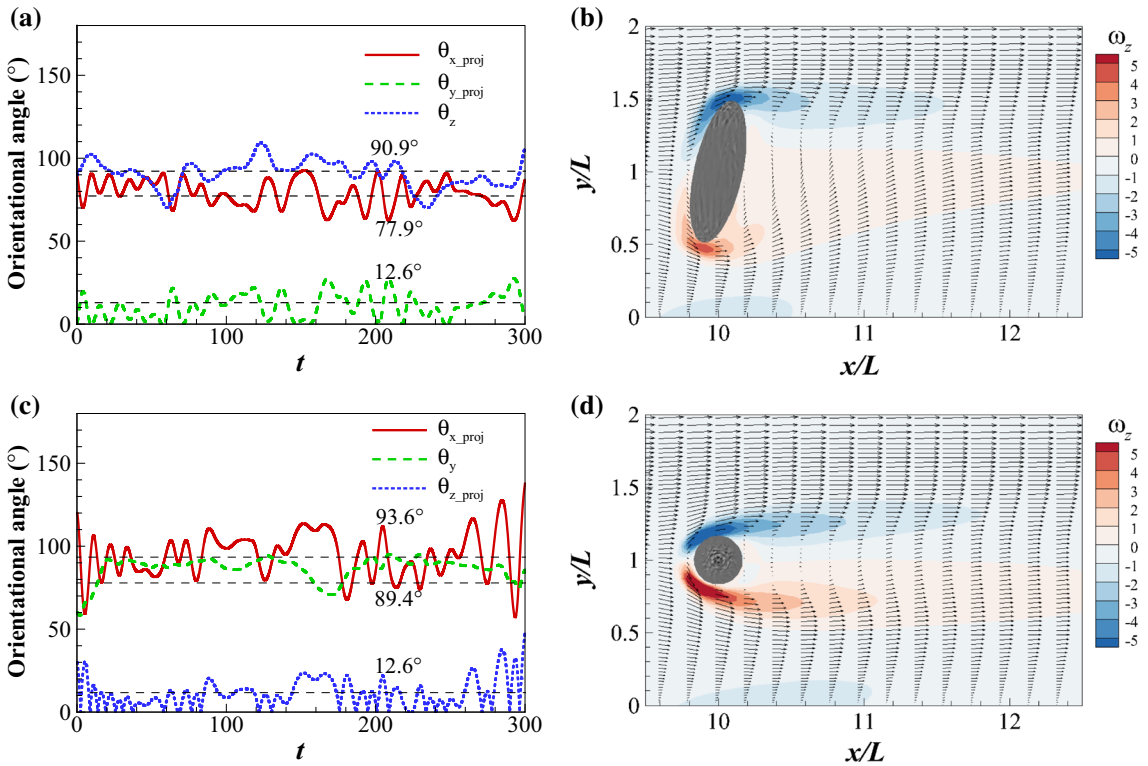

Fig. 13 **a**, **c** Orientation angles between the symmetry axis and the coordinates axes of the global coordinate system and **b**, **d** contours of the spanwise vorticity and velocity vectors in the $x - y$ plane for a prolate particle (AR $= 3$) located in the buffer region of the turbulent boundary layer. **a** and **b** are related to the steady mode 1 with its symmetry axis close to the y-axis; **c** and **d** are related to the steady mode 2 with its symmetry axis close to the z-axis

positioned near the spanwise direction, i.e., cases 3a and 5a in Table 4, its symmetry axis is preferentially aligned in the spanwise direction, as shown in Fig. 13c for case 3a.

From the above results, it is seen that with different initial orientations, listed in Table 4, the oblate particles all converge to the same steady motionless state. For the particle placed in the buffer layer ($y_P = L$ or $y_P^+ = 18.1$), the relative velocity at the particle center U_P is about 0.5, and the averaged shear rate G is $0.2 \sim 0.3$ within the volume the particle is occupying, which all match the setting in Sect. 3.3 for the linear shear flow. The average motions for both prolate and oblate particles in the near-wall region of turbulence are similar to those in a linear shear flow, and it is seen that the turbulent fluctuation in the near-wall region has an insignificant effect on the finite-sized particles' motion.

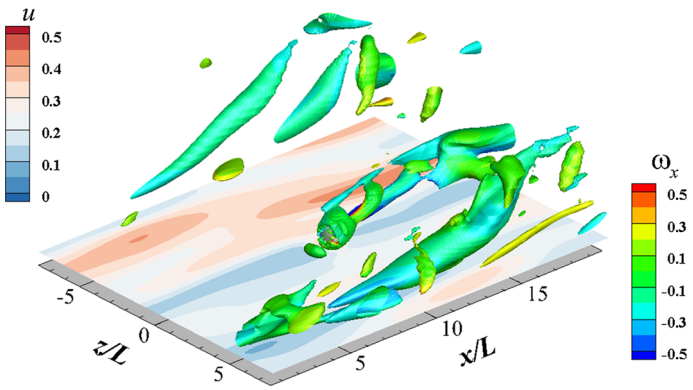

Fig. 14 Instantaneous vortical structures of the near-wall turbulence around an oblate particle (AR $= 1/3$) located in the buffer region. The iso-surface of Q $= 0.01$ is flooded by the streamwise vorticity ω_x. The contour of streamwise velocity is displayed in blue/red in the $x - z$ plane at $y^+ = 3$. The particle center is located at $(10L, L, 0)$ in the buffer region

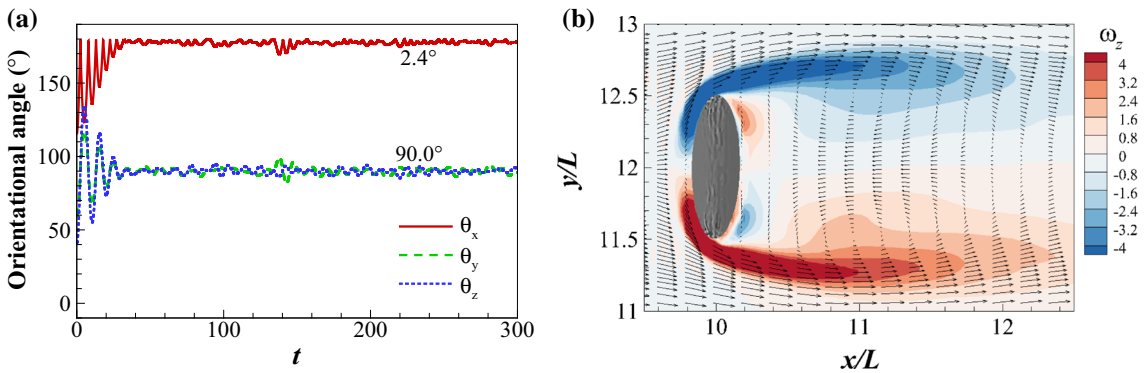

Fig. 15 **a** Orientation angles between the symmetry axis and the coordinates axes of the global coordinate system, and **b** contours of the spanwise vorticity and velocity vectors in the $x - y$ plane for an oblate particle (AR $= 1/3$) located outside of the turbulent boundary layer

When an oblate particle or a prolate particle is positioned outside of the boundary layer, the turbulent fluctuations and the shear almost vanish. Figure 15 shows the results of case 3b for the oblate particle, while Fig. 16a, c shows the results for the prolate particle of cases 1a and 3a, respectively. It is observed that the amplitude variation in the orientation angle is much smaller than in the buffer region, and the average orientations of the particles are quite similar to those in a uniform flow.

4 Conclusions

In the present study, the rotational dynamics of a finite-sized ellipsoidal particle in different fluid flows has been investigated by direct numerical simulation. The particle is fully resolved by the immersed boundary projection method (IBPM), and its motion is governed by Euler's equation and is computed in the body-fixed frame. The rotational motion of an ellipsoid in Couette flow at low Re_P and in a uniform cross-flow with different solid-to-fluid density ratios at intermediate Re_P is simulated. Good agreement between the present results and those from previous studies validates the present numerical method in solving the rotational motion of a finite-sized particle in viscous fluid.

The prolate and oblate particles are freely rotating in uniform flow, linear shear flow, and wall-bounded turbulence, with their centers fixed. In a uniform flow, the oblate particle converges to a motionless steady state, where its symmetry axis points in the streamwise direction with a maximum drag force independent of the initial orientation. On the other hand, the prolate particle tends to two different steady orientations with a maximum drag force, either aligning its symmetry axis to the wall-normal direction or the spanwise direction, depending on the initial orientation. Also, a linear stability analysis is performed to confirm the steady state of different ellipsoids in a uniform flow. For an ellipsoid rotating in a linear shear flow, the steady state can be regarded as a nonlinear combination of those in uniform flow and Couette flow, reflected through the effects of

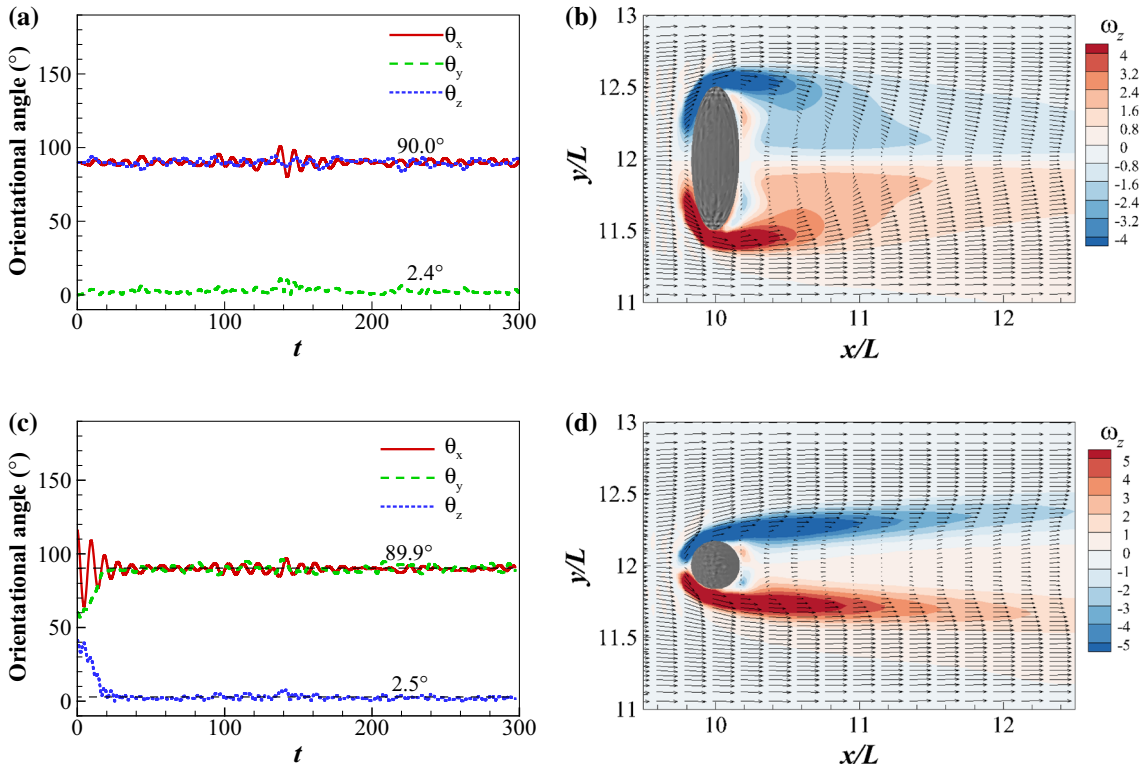

Fig. 16 **a**, **c** Orientation angles between the symmetry axis and the coordinates axes of the global coordinate system, and **b**, **d** contours of the spanwise vorticity and velocity vectors in the $x - y$ plane for a prolate particle (AR $= 3$) located outside of the turbulent boundary layer. **a** and **b** are related to the steady mode 1 with its symmetry axis aligned with the y-axis direction; **c** and **d** are related to the steady mode 2 with its symmetry axis aligned with the z-axis

fluid inertia and fluid shear. In most occasions, the fluid inertia dominates the dynamics of the ellipsoids. The steady states for both the prolate and oblate particles are characterized by the slight inclination of the major axes of the particles from the flow-gradient plane with a large drag force. By changing the shear rate G or the relative velocity at the particle center U_{P}, the effects of fluid shear and inertia shear have been analyzed separately. The fluid inertia increases with U_{P}, leading to a smaller inclined angle, which converges to the steady state in cross-flow, while increasing the fluid shear G leads to a larger inclined angle, which is close to the steady state in Couette flow. When increasing the fluid viscosity, the shear stress also increases, causing a larger inclined angle. For wall-bounded turbulence, the particle located in the buffer zone has an average motionless steady state similar to that in the linear shear flow, while the particle located outside of the boundary layer is similar to that in the uniform flow. This shows that turbulent fluctuations have no significant effect on the average motion of finite-sized ellipsoids. The present results on a finite-sized particle rotating in flows with an intermediate to large Re_{P} can be regarded as a starting point for understanding the dynamics of heavy (solid-to-fluid density ratio in the order of $10^2 \sim 10^3$) finite-sized particles in viscous fluid flows.

Acknowledgements The work was supported by National Natural Science Foundation of China under Grants Numbers 11490551, 11772172 and 11702158. The authors would like to thank Tsinghua National Laboratory for Information Science and Technology for support in parallel computation.

Appendix

The two-dimensional motion of a nonspherical particle can be expressed as

$$\begin{aligned} I\frac{\mathrm{d}\omega'}{\mathrm{d}t} &= M\left(\omega', \varphi\right), \\ \frac{\mathrm{d}\varphi}{\mathrm{d}t} &= \omega' \end{aligned} \tag{A1}$$

Table 5 Fitted coefficients for the pitching torque and rotational torque by Zastawny et al. [37]

Fitted Coefficients	Oblate (AR = 1/5)	Prolate 1 (AR = 5/2)	Prolate 2 (AR = 5/4)
c_1	3.782	2.078	0.935
c_2	0.237	0.279	0.146
c_3	0.351	0.372	− 0.469
c_4	0.236	0.018	0.145
c_5	− 0.394	0.98	0.116
c_6	1.615	0.0	0.748
c_7	− 0.044	0.0	0.041
c_8	− 0.537	1.0	0.221
c_9	1.805	0.0	0.657
c_{10}	− 0.037	0.0	0.044
d_1	13.31	71.03	1.244
d_2	0.189	0.069	0.239
d_3	783.05	773.04	378.12
d_4	0.628	0.67	0.789

where ω' denotes the angular velocity in the body-fixed frame, φ denotes the angle between the major axis and the streamwise direction, I is the moment of inertia, and $M\left(\omega', \varphi\right)$ is the torque function in the body-fixed frame.

For implementation of the linear stability analysis, an empirical formulation of the torque term M for a nonspherical particle in the uniform flow proposed by Zastawny et al. [37] is adopted, i.e.,

$$I\dot{\omega} = \frac{C_T}{16}\rho\pi L^3 \left|\tilde{\mathbf{u}}\right|^2 + C_R\frac{\rho}{2}\left(\frac{L}{2}\right)^5 |\mathbf{\Omega}|\,\Omega, \tag{A2}$$

$$C_T = \left(\frac{c_1}{Re_P^{c_2}} + \frac{c_3}{Re_P^{c_4}}\right)\sin(\varphi)^{c_5+c_6\mathrm{Re}_P^{c_7}}\cos(\varphi)^{c_8+c_9\mathrm{Re}_P^{c_{10}}}, \tag{A3}$$

$$C_R = d_1\left(Re_R\right)^{d_2} + \frac{d_3}{Re_R^{d_4}} \tag{A4}$$

where L denotes the major diameter of the nonspherical particle, ρ is the fluid density, and C_T and C_R represent the coefficients of pitching torque and rotational torque, respectively. Moreover, $\tilde{\mathbf{u}} = \mathbf{u} - \mathbf{u}_C$ and $\mathbf{\Omega}=\frac{1}{2}\nabla\times\mathbf{u} - \boldsymbol{\omega}'$ are the relative velocity at the particle center and the relative angular velocity, respectively. In the above equations, the particle Reynolds number Re_P is defined based on the uniform flow velocity, while Re_R is the rotational Reynolds number, defined as $Re_R=L^2\left|\mathbf{\Omega}\right|/\nu$. The formula of the torque coefficients, i.e., Eqs. (A3) and (A4), is fitted from a series of DNS results with different shaped spheroidal particles fixed in cross-flow with a definite incident angle. The fitted coefficients obtained by Zastawny et al. [37] are listed in Table 5. It should be noted that the numerical simulations in Zastawny et al. [37] are in three dimensions, while the particle obeys a two-dimensional motion with its symmetry axis located in the $x - y$ plane.

According to the linear stability analysis theory [29], perturbation of Eq. (A1) is expressed as

$$\frac{\mathrm{d}}{\mathrm{d}t}\begin{bmatrix}\delta\omega'\\ \delta\varphi\end{bmatrix} = \begin{bmatrix}\frac{\partial M^-}{\partial\omega'} & \frac{\partial M^-}{\partial\varphi}\\ 1 & 0\end{bmatrix}\begin{bmatrix}\delta\omega'\\ \delta\varphi\end{bmatrix}. \tag{A5}$$

For convenience, we note

$$M^-_{\omega'} = \frac{\partial M^-}{\partial\omega'};\ M^-_{\varphi} = \frac{\partial M^-}{\partial\varphi} \tag{A6}$$

where the superscript '-' indicates that the torque function M is scaled by the moment of inertia I. For calculating $M^-_{\omega'}$ and M^-_{φ}, the numerical method is adopted rather than the analytical method since the coefficients are obtained by numerical fitting. Here, the torques are calculated at 10 different angular positions and angular velocities with a small increment 0.001 near the equilibrium position and are fitted by the least squares method. Then the partial derivatives of the pitching torque and rotational torque are obtained accordingly.

From the perturbation Eq. (A5), we have a solution form of

$$\delta\omega' = \delta\omega'_0 e^{\lambda_1 t},\quad \delta\varphi = \delta\varphi_0 e^{\lambda_2 t} \tag{A7}$$

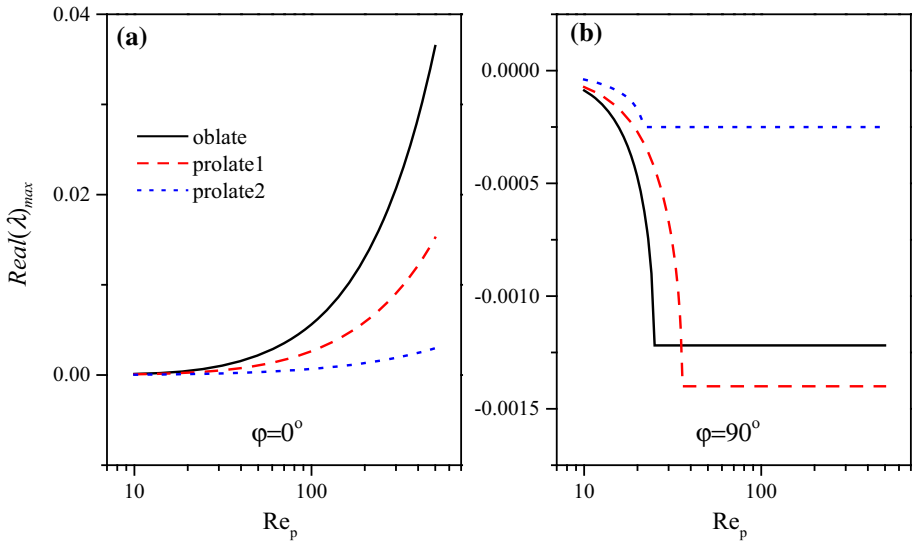

Fig. 17 Variation in the maximum real part of the eigenvalues $\lambda_{1,2}$ with the Reynolds number for two equilibrium states: **a** $\varphi = 0°$; **b** $\varphi = 90°$

where $\left[\delta\omega_0' \ \delta\varphi_0\right]$ denotes the initial perturbations, and $\lambda_{1,2}$ denotes the eigenvalues of the coefficient matrix in Eq. (A5), i.e.,

$$\lambda_{1,2} = \frac{M_{\omega'}^{-} \pm \sqrt{M_{\omega'}^{-2} + 4M_{\varphi}^{-}}}{2}. \tag{A8}$$

If the system is stable, the real parts of $\lambda_{1,2}$must be negative, which requires $M_{\omega'}^{-} < 0$ and $\left|M_{\omega'}^{-}\right| > \sqrt{M_{\omega'}^{-2} + 4M_{\varphi}^{-}}$. Hence, the stablility condition of the linear system is obtained, i.e.,

$$M_{\omega'}^{-} < 0, \ M_{\varphi'}^{-} < 0. \tag{A9}$$

In the following, two equilibrium states, i.e., $\varphi = 0°$ and $\varphi = 90°$, are considered, and both have zero initial angular velocity. For simplicity, the fluid vorticity at the particle center is assumed to be zero in calculating the relative angular velocity, which can be verified by the symmetry distribution of the vorticity field, as shown in Figs. 3 and 4. Figure 17 presents variations in the maximum real part of the eigenvalues $\lambda_{1,2}$, which represents the growth rate of the linear system under infinitesimal perturbations, with the particle Reynolds number Re_{P}. For $\varphi = 0°$ (see Fig. 17a), the maximum real parts of the eigenvalues are all positive for both the oblate and prolate particles, but become all negative for $\varphi = 90°$ as seen in Fig. 17b. Hence, it confirms that the equilibrium state $\varphi = 0°$ is unstable, while the equilibrium state $\varphi = 90°$ is stable within a wide range of Re. It should also be noted that the Reynolds number range, where the above linear stability analysis is performed, also depends on the validity range of the torque formulation in Eqs. (A2)–(A4).

References

1. Ardekani, M.N., Costa, P., Breugem, W.P., Brandt, L.: Numerical study of the sedimentation of spheroidal particles. Int. J. Multiph. Flow **87**, 16–34 (2016)
2. Ardekani, M.N., Costa, P., Breugem, W.P., Picano, F., Brandt, L.: Drag reduction in turbulent channel flow laden with finite-size oblate spheroids. J. Fluid Mech. **816**, 43–70 (2016)
3. Brenner, H.: The Stokes resistance of an arbitrary particle—IV arbitrary fields of flow. Chem. Eng. Sci. **19**(10), 703–727 (1964)
4. Challabotla, N.R., Nilsen, C., Andersson, H.I.: On rotational dynamics of inertial disks in creeping shear flow. Phys. Lett. A **379**(3), 157–162 (2015)
5. Challabotla, N.R., Zhao, L., Andersson, H.I.: Shape effects on dynamics of inertia-free spheroids in wall turbulence. Phys. Fluids **27**(6), 143 (2015)

6. Challabotla, N.R., Zhao, L.: Andersson H I. Orientation and rotation of inertial disk particles in wall turbulence. J. Fluid Mech. **766**, R2 (2015). https://doi.org/10.1017/jfm.2015.38
7. Challabotla, N.R.: Nonspherical particle suspensions in wall turbulence. Ph.D. thesis. Norwegian University of Science and Technology, Norway (2016)
8. Clift, R., Grace, J.R., Weber, M.E.: Bubbles, Drops, and Particles. Academic Press, Cambridge (1978)
9. Ding, E.J., Aidun, C.K.: The dynamics and scaling law for particles suspended in shear flow with inertia. J. Fluid Mech. **423**(423), 317–344 (2000)
10. Eshghinejadfard, A., Abdelsamie, A., Hosseini, S.A., Thévenin, D.: Immersed boundary lattice Boltzmann simulation of turbulent channel flows in the presence of spherical particles. Int. J. Multiph. Flow **96**, 161–172 (2017)
11. Eshghinejadfard, A., Hosseini, S.A., Thévenin, D.: Fully-resolved prolate spheroids in turbulent channel flows: a lattice Boltzmann study. AIP Adv. **7**(9), 095007 (2017)
12. Huang, W.X., Chang, C.B., Sung, H.J.: Three-dimensional simulation of elastic capsules in shear flow by the penalty immersed boundary method. J. Comput. Phys. **231**(8), 3340–3364 (2012)
13. Huang, H., Yang, X., Krafczyk, M., Lu, X.Y.: Rotation of spheroidal particles in Couette flows. J. Fluid Mech. **692**(692), 369–394 (2012)
14. Jeffery, G.B.: The motion of ellipsoidal particles immersed in a viscous fluid. Proc. R. Soc. Lond. **102**(715), 161–179 (1922)
15. Kempe, T., Schwarz, S., Fröhlich, J.: Modelling of spheroidal particles in viscous flows. In: Proceedings of the Academy Colloquium Immersed Boundary Methods: Current Status and Future Research Directions (KNAW, Amsterdam, The Netherlands), 15–17 (2009)
16. Kempe, T., Vowinckel, B., Fröhlich, J.: On the relevance of collision modeling for interface-resolving simulations of sediment transport in open channel flow. Int. J. Multiph. Flow **58**(1), 214–235 (2014)
17. Kim, K., Baek, S.J., Sung, H.J.: An implicit velocity decoupling procedure for the incompressible Navier–Stokes equations. Int. J. Numer. Methods Fluids **38**, 125–138 (2002)
18. Ku, X.K., Lin, J.Z.: Inertial effects on the rotational motion of a fibre in simple shear flow between two bounding walls. Physica Scripta **27**(80), 025801 (2009)
19. Larson, R.G., Ottinger, H.C.: Effect of molecular elasticity on out of-plane orientations in shearing flows of liquid-crystalline polymers. Macromolecules **24**(23), 6270–6282 (1991)
20. Li, R.Y., Xie, C.M., Huang, W.X., Xu, C.X.: An efficient immersed boundary projection method for flow over complex/moving boundaries. Comput. Fluids **140**, 122–135 (2016)
21. Lund, T.S., Wu, X., Squires, K.D.: Generation of turbulent inflow data for spatially–developing boundary layer simulations. J. Comput. Phys. **140**(2), 233–258 (1998)
22. Lundell, F., Carlsson, A.: Heavy ellipsoids in creeping shear flow: transitions of the particle rotation rate and orbit shape. Phys. Rev. E Stat. Nonlinear Soft Matter Phys. **81**(2), 016323 (2010)
23. Mao, W., Alexander, A.: Motion of spheroid particles in shear flow with inertia. J. Fluid Mech. **749**, 145–166 (2014)
24. Marchioli, C., Fantoni, M., Soldati, A.: Orientation, distribution, and deposition of elongated, inertial fibers in turbulent channel flow. Phys. Fluids **22**(3), 245 (2010)
25. Mortensen, P.H., Andersson, H.I., Gillissen, J.J.J., Boersma, B.J.: Dynamics of prolate ellipsoidal particles in a turbulent channel flow. Phys. Fluids **20**(9), 1211 (2008)
26. Mortensen, P.H., Andersson, H.I., Gillissen, J.J.J., Boersma, B.J.: On the orientation of ellipsoidal particles in a turbulent shear flow. Int. J. Multiph. Flow **34**(7), 678–683 (2008)
27. Peskin, C.S.: The immersed boundary method. Acta Numerica **11**, 479–517 (2002)
28. Qi, D., Luo, L.S.: Rotational and orientational behaviour of three-dimensional spheroidal particles in Couette flows. J. Fluid Mech. **477**(477), 201–213 (2003)
29. Redheffer, R.M., Port, D.: Differential Equations: Theory and Applications. Jones and Bartless, Burlington (1991)
30. Rosen, T., Do-Quang, M., Aidun, C.K., Lundell, F.: Effect of fluid and particle inertia on the rotation of an oblate spheroidal particle suspended in linear shear flow. Phys. Rev. E **91**, 053017 (2015)
31. Subramanian, G., Koch, D.L.: Inertial effects on fibre motion in simple shear flow. J. Fluid Mech. **535**(535), 383–414 (2005)
32. Subramanian, G., Koch, D.L.: Inertial effects on the orientation of nearly spherical particles in simple shear flow. J. Fluid Mech. **557**(557), 257–296 (2006)
33. Uhlmann, M.: An immersed boundary method with direct forcing for the simulation of particulate flows. J. Comput. Phys. **209**(2), 448–476 (2005)
34. Voth, G.A., Soldati, A.: Anisotropic particles in turbulence. Ann. Rev. Fluid Mech. **49**(1), 249–276 (2017)
35. Xia, Q.J., Huang, W.X., Xu, C.X., Cui, G.X.: Direct numerical simulation of spatially developing turbulent boundary layers with opposition control. Fluid Dyn. Res. **47**, 025503 (2015)
36. Yu, Z.S., Phan-Thien, N., Tanner, R.I.: Rotation of a spheroid in a Couette flow at moderate Reynolds numbers. Phys. Rev. E Stat. Nonlinear Soft Matter Phys. **76**(2), 026310 (2007)
37. Zastawny, M., Mallouppas, G., Zhao, F., Wachem, B.V.: Derivation of drag and lift force and torque coefficients for non-spherical particles in flows. Int. J. Multiph. Flow **39**, 227–239 (2012)
38. Zettner, C.M., Yoda, M.: The circular cylinder in simple shear at moderate Reynolds numbers: an experimental study. Exp. Fluids **30**(3), 346–353 (2001)